nature portfolio

https://doi.org/10.1038/s41567-022-01641-9

Supplementary information

Self-regulation of phenotypic noise synchronizes emergent organization and active transport in confluent microbial environments

In the format provided by the authors and unedited

SUPPLEMENTARY MATERIAL

Self-regulation of phenotypic noise synchronizes emergent organization and active transport in confluent microbial environments

Jayabrata Dhar,[1] Anh L. P. Thai,[1] Arkajyoti Ghoshal,[1] Luca Giomi,[2] and Anupam Sengupta[1,*]

[1] *Physics of Living Matter, Department of Physics and Materials Science, University of Luxembourg, 162 A, Avenue de la Faïencerie, L-1511 Luxembourg City, Luxembourg*

[2] *Instituut-Lorentz, Universiteit Leiden, P.O. Box 9506, 2300 RA Lieden, The Netherlands*

Keywords: microbial active matter, bacterial colonies, confluent cells, mono-to-multilayer transition, emergence, self-organization, active transport, multifield topology

A. Supplementary Text

1. Growth temperature is a proxy for activity

We use growth temperature (T) to tune the activity of confluent colonies at individual and colony-scales, varying it over ecologically-relevant values: 25°C, 30°C, and 37°C (see Methods, Section **??**). The choice of growth temperature as a parameter to tune the phenotypic parameters (Supplementary Table S1 and Figure S3) allowed us to regulate the active mechanics underpinning expansion of bacterial colonies over multiple generations (Supplementary Figure S3B). Quantitative imaging of individual cells across multiple generations, as shown in Figure **??**A-C (see Sections **??** and **??** for the tracking methods), revealed that $\tau_{\rm d}$, population doubling time decreased from (mean ± s.d.) 56.73 ± 2.28 min (44.9 ± 2.6 min) for Strain-1 (Strain-2) at 25°C to 24 ± 1.12 min (18.73 ± 0.85 min) at 37°C (Supplementary Figure S3C,D). Correspondingly, the rate of change of cell numbers (N), $\mathrm{d}N/\mathrm{d}t$, increased with temperature for both the *E. coli* strains. A similar dependence with temperature is captured also for individual cells, measured in terms of the cell length doubling time (τ_{sc}). Taken together, we could harness the growth temperature to tune the biophysical activity of expanding confluent bacterial layers, at both individual and population scales (Supplementary Figure S3C,D and F).

2. Phenotypic traits and at MTMT follow log-normal distribution

The temperature-dependent bacterial growth regulates the cell and colony phenotypes. As depicted in Supplementary Figure S3E for the cell length-at-birth, $\ell_{\rm b}$ (see Supplementary Figures S4 and S5 for image analysis), our results reveal a high variance in $\ell_{\rm b}$ across the temperatures considered here, in agreement with previous reports under homeostatic considerations [1, 2]. At MTMT, $\ell_{\rm b}$ showed a weak dependence on the growth temperature, with broad strain-specific distributions that peaked within the range of 1 μm – 5 μm for Strain-1 and between 1 μm and 5.5 μm for Strain-2 (Supplementary Figure S3E respectively). The difference between the peak values reduces as the temperate goes up: the peak at 25°C and 30°C differ conspicuously relative to the peak value at 37°C, however no detectable difference was captured between the peaks at 25°C and 30°C.

At MTMT ($t = t_{\rm c}$), the distribution of the cell aspect ratio, AR ($= \ell/w$, w being the bacterial width), shows high variance across all temperatures (Supplementary Figure S3A) and species considered (Supplementary Table S2). Though the PDFs do not reveal specific dependence on the growth temperature, the quantity $\log \mathrm{AR}$ exhibits a prominent Gaussian distribution (insets in Figure **??**E), that highlights the log-normal distribution of AR at MTMT. Over $0 < t < t_{\rm c}$, the mean AR drops as the colony ages (Supplementary Figure S6), while maintaining the log-normal nature of distribution. The reduction of mean AR has a two-fold consequence on the colony: smaller cell aspect ratio enhances the probability of MTMT onset [3]; and the number packing fraction (*i.e.*, the number of cells within a given area) goes up, leading to more efficient packing of cells. Consequently, growth-induced stresses upon a cell division event are higher at the colony center relative to the colony periphery. Together, the reduced mean AR and higher packing fraction enhance the probability of MTMT as time passes, such that the MTMT probability at a given time goes down radially from the center to the periphery. The log-normal nature of the cell $\ell_{\rm b}$ and AR is observed frequently in natural systems, stemming from the underlying independent random variables [1, 2, 4, 5]. Our results suggests a link between the $\ell_{\rm b}$ and AR, which we confirm theoretically in Section **??** (Equation **??**a) to show that the probability distribution of the AR is ultimately determined by the length-at-birth, as long as the strain-specific variability in growth rate remains low, validating previous experimental reports [6].

The areal speed of the colony, $\mathrm{d}A/\mathrm{d}t$, increased mono-

* anupam.sengupta@uni.lu

tonically with time, reaching a maximum at $t > t_c$, synchronously after the MTMT event, ultimately dipping to ~ 0 μm/s (Supplementary Figure S3F). The horizontal expansion is arrested as multiple layers emerge (Supplementary Figure S17). The maximum dA/dt increases with the temperature, whereas the time taken to attain the peak speed depends inversely on the growth temperature. The maximum dA/dt dropped 4-fold for Strain-1, from 2284 μm^2/h to 572 μm^2/h, as temperature dropped from 37°C to 25°C (left panel, Supplementary Figure S3F), for the Strain-2 (Supplementary Figure S3F, right panel), the reduction was 2-fold, from 1455 μm^2/h to 685 μm^2/h. Overall, enhanced biophysical activity accelerates the sequence of events in an expanding colony, as evidenced by the time interval shortening between the MTMT and the $(dA/dt)_{max}$ (inset, Supplementary Figure S3F). For Strain-1, the time interval increases from 175 min. at 37°C to 88 min. at 25°C.

3. *Cell-cell phenotypic noise suppresses variability of inter-colony traits*

Variability of cellular traits emerges over time as confluent colonies expand. Focusing on the variation of AR, and the resulting noise, we demonstrate that a gain in the phenotypic noise over time promotes uniformity of colony-scale traits (*i.e.*, traits measured across different colonies). Such a trend–observed in different species and growth conditions we span–suggests its generality. Figure S1A presents two distinct colonies of Strain-1, growing under same conditions, at specific growth points. Initially, At $t = 3$ min, the AR noise within single-celled (or two-celled) colonies arise due to the intrinsic variability, which grows as the colony expands (Figure S1B). The cell-cell AR variability for a given colony emerges due to an interplay between the growth rate of individual cells and their length-at-birth, ℓ_b, both of which are intrinsically stochastic. Since the cell number growth rate k_n is larger than single cell length growth k_{sc} (Figure S3, [7]), as time progresses, cells reduce their AR due to relatively faster division than cell elongation, ultimately resulting in lower mean AR for both (or all) colonies ($t = 240$ min, 225 min; Figures S1A (inset), S1C, and S6). The results indicate that phenotypic traits diversify at the individual scale–a signature of optimal growth [8]–while inter-colony noise at the population scale reduces as colonies approach MTMT (Figure S1C).

Starting from a given AR, cells within a colony diversify their morphological traits as the colony expands (Figure S1B), approaching log-normal distribution at MTMT underpinned by the inherent log-normal nature of the length-at-birth (see Eq. **??** and Figure S3). This signifies amplification of phenotypic noise at individual scales closer to the MTMT events (Figure S3A). Figure S1B presents the AR noise and its variability as colonies expand, showing a maximum close to the MTMT event.

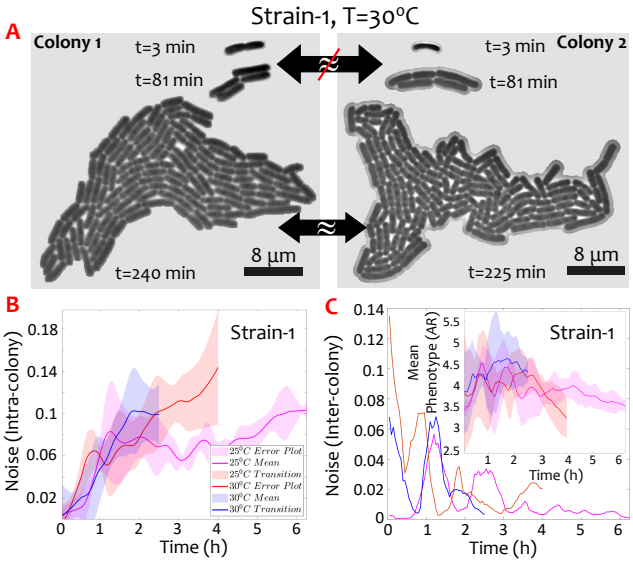

FIG. S1. **Gain in cell-cell phenotypic noise suppresses inter-colony variability.** **(A)** Cellular phenotypic noise increases within a confluent bacterial colony as it expands, shown here till MTMT for Strain-1 AR at 30°C. Overall, at a particular temperature, intrinsic stochasticity drives increment of cell-scale variability within each of the growing colonies. However, noise across colonies reduces, *i.e.*, similar AR emerges across confluent colonies over time due to the overall log-normal distribution of ℓ_b. **(B)** Temporal variation of cell-cell AR noise within Strain-1 colonies (Strain-2 in Figure S10A). Shaded region presents error about the mean AR in the colony. **(C)** Temporal variation of AR inter-colony noise for Strain-1 for different temperatures (Strain-2 data in Figure S10B), computed from the variance across three biological replicates. Inset: The temporal variation of mean and error of the AR across colonies. The inter-colony mean AR decreases as the colony approaches the MTMT. The inter-colony noise, as shown in the main plot, is estimated using the mean and variance of AR in the inset.

The corresponding variation of ℓ_b shown in Figures S10 (panels C and D) render the colony-scale traits statistically comparable at onset of the MTMT event. Overall, as the intra-colony variability increases, following a log-normal distributions, the inter-colony variability reduces, thus indicating that the gain in noise within each colony makes the way for suppression of noise across the colonies. As we have shown previously, the statistics of the cell length can be determined by the statistics of the length at birth ℓ_b (Eqs. **??** and **??**). The log-normal nature of ℓ_b introduces the inherent noise in the cell length (or AR), and because the number of cells increases in time, all cumulative quantities will have a variance that also grows in time, *i.e.*, the phenotypic noise within a colony increases. Now using the central limit theorem, we have $X = \sum_{i=1}^{N} x_i$ with x_i a set of independent random variables having the same mean μ and variance σ^2, we could write $\langle X \rangle = N\mu$ and $\mathrm{var}\, X = N\sigma^2$. Consequently, as $t \gg \tau_d$, *i.e.*, for $N \gg 1$, the noise $F(X) = (\sigma/\mu)^2 N^{-1}$ progressively reduces across colonies. We emphasize that,

in addition to the log-normal statistics (ℓ_b and AR), the rod-shaped morphology and the temperature-dependent growth rate regulate the statistically precise onset of the MTMT event (t_c), thereby establishing the topological manifestations and the time-synchronous active transport properties across confluent colonies.

4. *Biological relevance of well-timed MTMT events and emergent active transport in confluent colonies*

The cross-talk between noisy phenotypic traits co-emerging in confluent bacterial colonies results in a mitigating effect, that ultimately underpins temporal correlations between structural changes (MTMT) and the emergence of active transport in the bacterial micro-environment. Our results, confirmed for different bacterial species and growth conditions (temperature and nutrient levels), demonstrate the generality of the structure-flow-transport nexus in confluent bacterial systems, with potentially far-reaching ramifications in diverse microbial, cellular and bio-engineered systems of higher complexity. Functionally, high cellular noise can limit coordinated cellular responses to environmental signals, however it can also enhance the adaptive behavioural traits due to the diversification of the cellular responses [9]. While cell-to-cell variability has been viewed as information within multi-cellular organisms [10], our work provides the first evidence and mechanistic framework for noise-mediated biophysical information cascade in unicellular settings. Below, we briefly describe the potential implications of (i) well-timed MTMT events, and (ii) emergent micro-scale active transport, the two key conclusions we have reported in this work.

Biological relevance of well-timed MTMT events

The ability of bacteria to communicate between cells is well-established in the framework of quorum sensing and vesicle-mediated communications. Yet, how neighbouring bacterial colonies communicate remains largely unknown. The well-defined timing of the MTMT events in disparate colonies suggest a strong temporal correlation, thus control over the MTMT timing could provide a biophysical approach to tune synchronous quorum (and other biochemical) sensing between colonies. This posits a temporal correlation between biophysical and biochemical communications, which is yet to be explored. The role of quorum sensing, in addition to biofilm formation, is well-recognized in triggering drug-resistant phenotypes (for instance, antibiotic-resistant *persister* phenotypes [11]). Consequently, the well-defined timing of extrusion events–a proxy to quorum-like sensing between the colonies–could determine the biological selection of the resistant phenotypes.

As indicated through the small selection of examples above, synergy between colonies is expected to emerge, before individual colonies merge to generate a continuous biofilm structure. Although chemical communication between physically distant colonies are yet to be uncovered, noise-mediated time-synchrony indicates the existence of one, which may further dictate the behavioural fate of the newly formed biofilm. Such inter-colony communication and emergent synchrony have been reported across yeast colonies [12]. It however remains to be understood if and how disruption of the inter-colony synchrony *i.e.*, upon enhancement of noise associated with the MTMT timing (for instance, due to fluctuating nutrient or temperature fields) could impact the biological fitness and viability.

Beyond mono-species systems, the time-synchronous structure-flow-transport attributes can provide fundamental insights of developmental and evolutionary significance. The phenomenon of monolayer-to-multilayer transition is not restricted to confluent bacterial species alone: it is exhibited by diverse poly-microbial communities found commonly in humans and plants (also known as microbiome [13]), and in multi-cellular systems like epithelial tissues [14]. Despite the biological complexity of such systems, the spatio-temporal coordination of morphogenesis is underpinned by analogous biomechanical interactions [15]. Thus, temporal association between morphological transitions and emergent transport of molecular and micro-cargo is expected to play an important role therein.

Biological relevance of active transport in sessile colonies

Our *in vitro* and *in silico* results reveal that the active microflows generated by expanding colonies are strong enough to enhance the local transport of molecular and material cargo spanning sub-microns to micron in size. Numerical results reported here show that under high viscous settings, as is often the case within biofilms colonizing surfaces, the colony-generated flows can transport sub-micron particles overcoming the Brownian motion. Biologically relevant micro-cargo are ubiquitous in bacterial colonies: co-existing bacterial cells [13, 16, 17], fungal spores [18], liposomes [19] and extracellular vesicles [20] delivering genetic cargo, and hitchhiking bacteriophages enhancing carrier bacteria colonization [21]. Transport of biological cargo by collective bacterial effects reported so far relies either on the bacterial motility or on their ability to elicit collective swarming behaviour. Our results extend the current transport paradigm by demonstrating how non-motile sessile phenotypes can drive enhanced transport by harnessing structural transitions. Such structure-transport properties of non-motile species will shed light on the co-evolution of carrier and cargo entities exposed to different selection pressures, particularly in the context of stability and resilience of synthetic and natural microbial consortia. Furthermore, emergent transport in engineered sessile systems can be harnessed toward development of drug delivery pipelines using synthetic beads and capsules in mammalian systems [22].

B. Supplementary Method

1. Cell culture protocol for additional species

In addition to the strains S-1 and S-2, we have validated the experimental results using two additional species: (i) *Serratia marcescens* PCI 1107, and (ii) nutrient-limited *Escherichia coli* NCM3722 delta-motA, both of which were grown under optimal growth temperatures (28^0C, and 37^0C respectively). The cells culture, and the samples for the time-lapse imaging experiments were prepared following the protocol outlined in the Methods Section **??**. For the nutrient-limited experiments, the nutrient concentration of the underlying substrate was reduced down to 25% of that used in the standard protocol (Section **??**). Supplementary Table S2 summarizes the phenotypic traits and corresponding noise of *S. marcescens* and nutrient-limited *E. coli* growing under optimal temperatures, in relation to the Strain-1 and Strain-2 data. The supplementary data validates results obtained from Strains 1 and 2, and confirms that the MTMT event is indeed statistically precise, despite high noise in the individual traits.

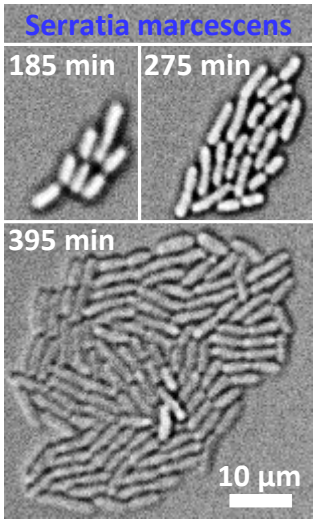

FIG. S2. **Growth and MTMT of *Serratia marcescens*.** In contrast to the Strains 1 and 2, the optimal growth temperature for for *S. marcescens* is 28^0C. *S. marcescens* is a distinct species with significantly longer doubling time, see Supplementary Table S2 for comparitive values, yet they validate the key properties we report here: (a) statistically precise MTMT event, despite the (b) *noisy* phenotypic traits. The MTMT event is seen here at 395 minutes.

C. Supplementary Tables and Figures

This section provides a detailed explanation and protocols for the cell counting and doubling time analysis from various parameters, image processing and cell segmentation steps detailed through graphical presentation, defect identification and quantification, colony-scale measurements using particle image velocimetry (PIV) algorithms and analysis, phase-plots of vortex strength distribution, tracks of passive particles generated from data-based simulation with which MSD and velocity correlations are estimated, and discussion and quantification of the particle transport experiments. In addition, the Supplementary Table S1 gives a glossary of all the symbols used in the article for easy reference. The Supplementary Table S2 provides a summary of the phenotypic traits and noise at 37°C at the MTMT time point (t_c) for all the species and nutrient conditions considered here.

D. Supplementary Movies

(Movie S1) Videos **(A)**, **(D)** and **(G)** shows the raw image sequence of a growing bacterial colony for three respective temperatures of 37°C, 30°C and 25°C. The videos capture one colony for each temperature. Background noise and light reflections can be observed during the capture of the colony growth videos. In order to remove the unwanted noise, the segregation of the bacterial colony must be performed. The extracted single colony evolution with time for each 37°C, 30°C and 25°C is shown in **(B)**, **(E)** and **(H)**, respectively. These extracted images are used as input for the PIV analysis. The video for the evolving velocity field due to the bacterial colony growth is presented in **(C)**, **(F)** and **(I)**, respectively, for 37°C, 30°C and 25°C. From the velocity field magnitude, we observe that at 37°C the colony shows highest hydrodynamic activity reflected by highest velocity magnitude. Furthermore, the velocity field vanishes outside the bacterial colony is due to the initial colony extraction performed on the raw images.

(Movie S2) Movie shows the evolution of the bead positions and their trajectory for **(A)** 37°C and **(B)** 25°C. The trajectories (for each colonies) obtained from such analysis is used to evaluate the MSD and diffusion coefficient of the bead transport. One important aspect which is apparent in the movies is the breakage of the particle agglomeration. **(C)** Control study on particle clusters in absence of bacterial colony reveal lack of de-clustering over long-times. Brownian motion alone, however, remains incapable of breaking the particle agglomeration. Thus, the present phenomena delineates that even for comparatively lower viscosity bacterial motion become biologically significant for agglomerated large molecules. Nevertheless, for non-agglomerating particles, the phenomena will reveal different outcome. We plan for further experiments to learn the effect of inter-particle interaction on bacterial motion-driven transport and understanding the significance of the outcome on biologically relevant situations.

TABLE S1. Glossary of symbols used in the study.

Parameter	**Units**	**Symbol**
Statistical Parameters		
Mean	unit specific	μ_0
Standard deviation (STD)	unit specific	σ_0
Mean of log of dimensionless length	1	μ
STD of log of dimensionless length	1	σ
Phenotypic noise	1	F
Packing fraction	1	ϕ
Coordination number	1	CN
Bounding ellipse major axis	m	a
Bounding ellipse minor axis	m	b
Normalized bounding area	1	A_{P}
Cluster circularity	1	b/a
Probability density function	1	PDF
Physical Parameters		
Temperature	°C	T
Pressure	N/m^2	P
Velocity field	m/s	$\boldsymbol{v}$ (U, V, W)
Critical force	N	f_{c}
Mean averaged vortex	m^2/s	MAV
Kinetic Drag coefficient	Pas/m^2	ζ
Effective Diffusion coefficient (for first layer)	m^2/s	$D_{z=z_1}$
Effective Diffusion coefficient (for second layer)	m^2/s	$D_{z=z_2}$
Brownian Diffusion coefficient	m^2/s	D_B
Mean Squared Displacement	m^2	MSD
Substrate-cell adhesive stiffness per unit length	$N/(ms^2)$	k_{a}
Cell and Colony Parameters		
Number of cells	1	N
Cell aspect Ratio	1	AR
Bacteria length	m	ℓ
Bacteria width	m	w
Bacteria length-at-birth	m	ℓ_{b}
Spherical cap area	m^2	A_{cap}
Length scale	m	ℓ_{a}
Instantaneous colony area	m^2	A
Critical area (colony area at MTMT)	m^2	A_{c}
Critical time (time to MTMT)	s	t_{c}
Time at peak (of hydrodynamics and transport)	s	t_{p}
Instantaneous area of single-cell	m^2	A_{sc}
Initial area of colony	m^2	A_0
Colony area growth rate	s^{-1}	k_{d}
Colony area doubling time	s	τ_{d}
Cell number growth rate (population growth rate)	s^{-1}	k_{n}
Cell number doubling time	s	τ_{n}
Cell elongation rate	s^{-1}	k_{sc}
Cell length doubling time	s	τ_{sc}
Number of defects	1	N_{d}
Defect concentration	m^{-2}	C_{d}

TABLE S2. Phenotypic traits and noise at MTMT for 37°C

Species	$t_{\mathrm{c}}(min)$	**Noise** t_{c}	$A_{\mathrm{c}} \times 10^{-4}(mm^2)$	**Noise** A_{c}	AR	**Noise** AR	$\tau_{\mathrm{n}}(min)$	**Noise** τ_{n}
Strain-1	179 ± 6.2	0.0012	6.22 ± 1.03	0.0273	4.3 ± 0.24	0.0828 ± 0.055	24.07 ± 0.96	0.0016
Strain-2	156 ± 5.2	0.0011	9.46 ± 4.81	0.2588	2.97 ± 0.12	0.083 ± 0.011	18.73 ± 0.85	0.002
NCM3722 [a]	404 ± 22.4	0.003	7.1 ± 2.82	0.158	3.39 ± 0.19	0.066 ± 0.01	59.78 ± 8.17	0.0186
S. Marcescens [b]	370 ± 8.3	0.0005	13.9 ± 3.52	0.064	3.21 ± 0.15	0.094 ± 0.04	47.76 ± 1.75	0.0013

[a] experiments conducted at low nutrient conditions

[b] optimal growth temperature is 28°C

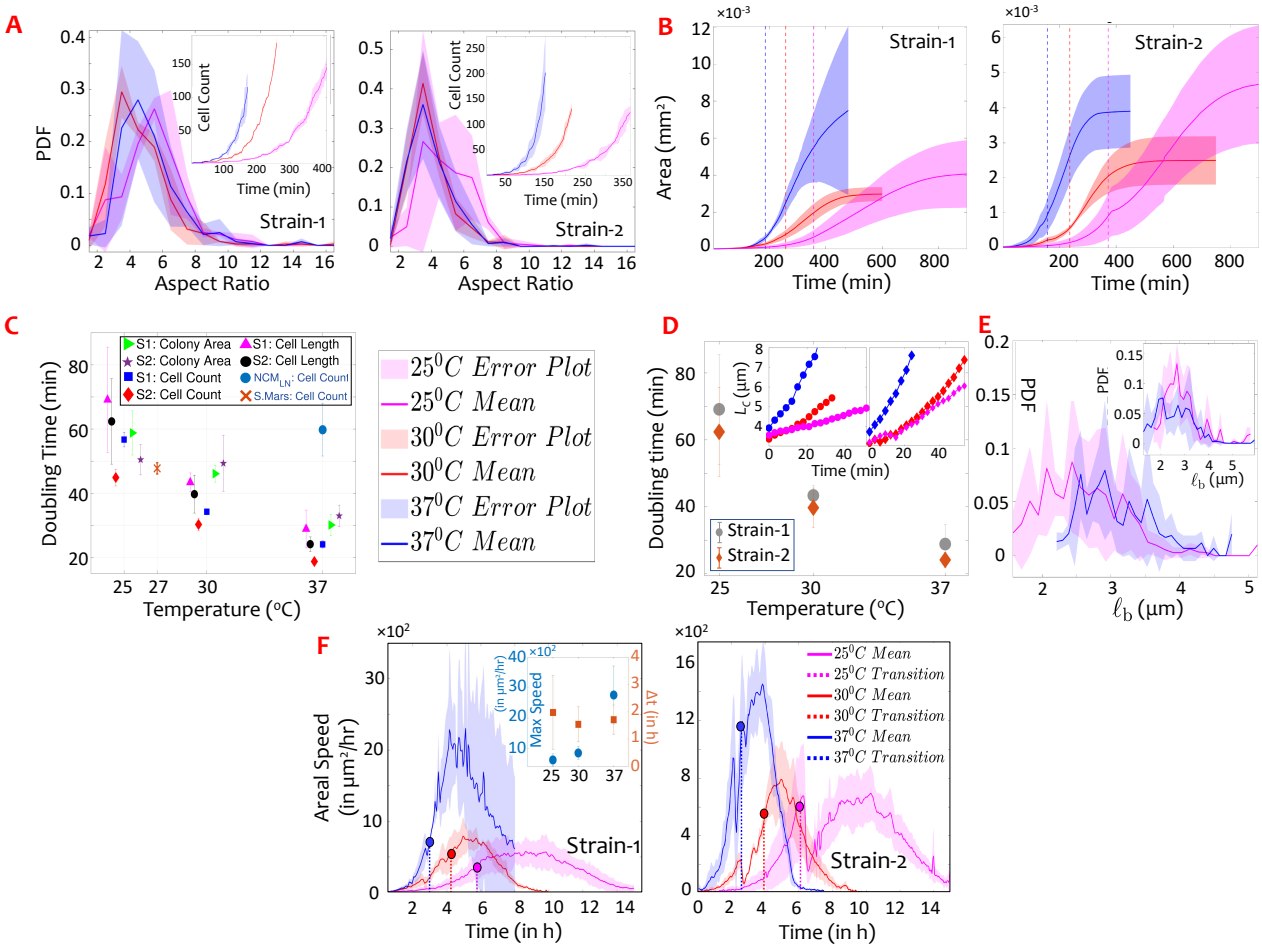

FIG. S3. **Growth and doubling parameters. (A)** AT MTMT, the PDF distribution of the cell AR, the shaded patch denotes the standard deviation and the mean is depicted by a solid line for Strain-1 (left panel) and Strain-2 (right panel). Inset: Depicts the corresponding growth for Strain-1 and Strain-2 at different temperatures. The growth efficacy increases with an increase in temperature, i.e. as the temperature approaches the optimum temperature of growth, which is 37^0C, the growth of the colony approaches its maximum potential to grow (keeping all other factors constant). **(B)** The evolution of colony area with time for each strain and temperature. The legend is same as in panel **(A)**. **(C)** The three different doubling time as obtained from single cell elongation, cell population growth and colony area growth are depicted in this figure. In addition, the doubling time for species E.coli NCM3722 delta-motA (grown under nutrient-limited conditions) and *Serratia marcescens*, under respective optimal growth temperatures, validate the experimental results. The observation of statistically precise MTMT timing, across species and growth conditions, suggest the generality of the results. The doubling time is obtained from the growth rate, which, in turn, is obtained from the exponential stage of the growth regime for cell population and colony area growth. The growth rate values extracted from these three phenomena remains in close proximity with each other signifying how one affects the other. The growth rate, a reflection of bacterial activity, increases with temperature, thus, posing temperature as the proxy for tuning ensuing biophysical, hydrodynamic and transport activity. At the colony-scale, the biophysical activity could be tuned systematically, with a ∼3-fold increase in the activity at 37°C relative to that at 25°C. Commensurating this, the time required to double the cell length was 28.87 ± 5.9 min (24.142 ± 2.26 min) for Strain-1 (Strain-2) at 37°C, increasing up to 43.39 ± 2.93 min (39.72 ± 5.9 min) at 30°C and to 69.13 ± 16.4 min (62.38 ± 13.3 min) at 25°C respectively (Figure **??**C and inset D). Supplementary section D **Movie S1** A, D and G show the evolution of bacterial colony (representative one replicate) for 37°C, 30°C and 25°C, respectively. **(D)** The population growth, intrinsically related to the cell elongation (Inset) and its rate, is a function of the growth temperature. Corresponding doubling times from the area growth and cell number are shown in Panel C. **(E)** At MTMT, the PDF of the length-at-birth for Strain-1 and Strain-2 (inset) capture a strong variance across all temperatures. **(F)** Evolution of the areal speed, $\mathrm{d}A/\mathrm{d}t$ (in μm^2/h) in an expanding bacterial colony, links the colony-scale geometry to the biophysical activity. The corresponding vertical dashed line indicates the incidence of the MTMT. Inset **(F)** The maximum areal speed (blue) increases as the temperature (hence growth rate) goes up, however the timing of the peak speed appear uncorrelated with the critical time (t_c), as indicated by the Δt (maroon) variation with the growth temperature.

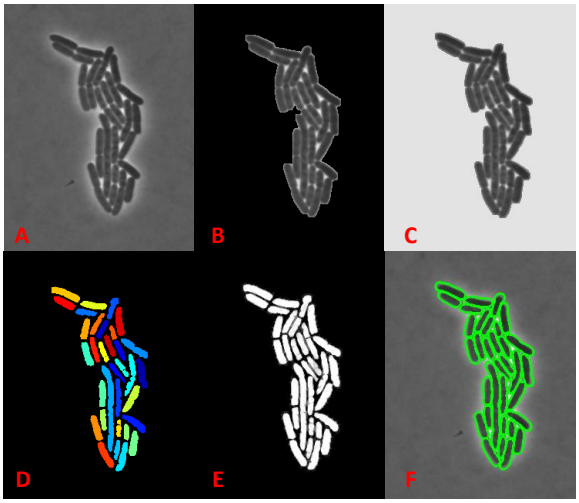

FIG. S4. **Cell segmentation and counting. (A - C)** The protocol for counting cells is established using a combination of AI-based Ilastik engine and MATLAB. First, MATLAB was used to pre-process the colony from **(A)** to **(C)**, which creates a strong contrast for better training and segmentation programming, details in Figure S5. **(B - D)** Ilastik was used for cell segmentation wherein numerous bacterial cells were used to train the model to properly differentiate between bacterial cells and the background. Once the segmentation labels were obtained, they were identified by MATLAB, followed by the identification, outlining and cell counting steps. The analyzed images were subjected to manual quality check to detect any discrepancy with the automated analysis pipeline. **(E - F)** Shows the segmented logical images of the cells and the logical image used to outline the cells overlayed on the raw image, respectively. These images gives the cell geometrical details.

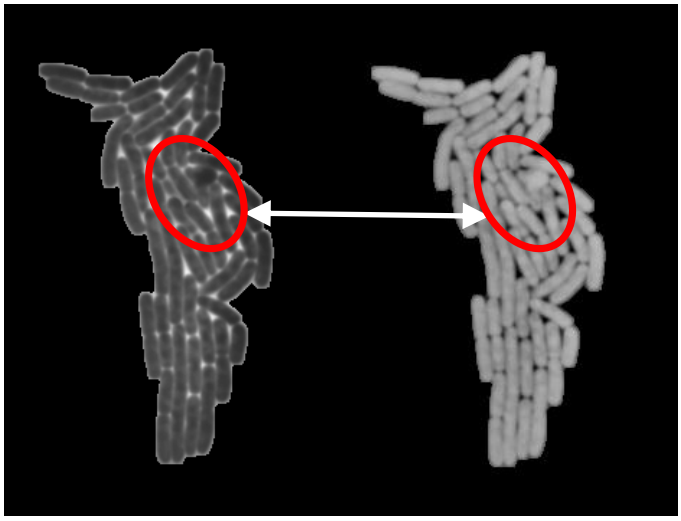

FIG. S5. **Tracking the onset of the mono to multilayer transition (MTMT) event.** The formation of a second-layer bacterial structure was identified through a series of image processing steps. In the left panel, we observe the extracted bacterial colony (at time 5.7 hours for a colony growing at 25°C). The right panel shows the colony after application of an image filter (described below) which clearly brings out the pattern of bacterial overlap, *i.e.*, a bacteria growing into a second layer situated at the top of the first layer. For the image filter, first the colony was extracted (Figure S4B), it segments the colony from the background (Figure S11). The background of Figure S4B is filled up with a colour that represents the near-whitish contrast of the bacterial cell and its immediate background (Figure S4C). Hereon, a combination of top-hat and bottom-hat filters are applied that eventually brings out the visually contrast of transitioning cells in the figure analyzed. One can clearly distinguish that the bacterial cells start growing on top of each other triggering the phenomenon of monolayer-to-multilayer transition. The present technique is used to extract the location of monolayer-to-multilayer transition along with the critical area and critical time that is used in Figure S1. All automated image analysis data were subject to manual quality checks, so as to rectify any discrepancy.

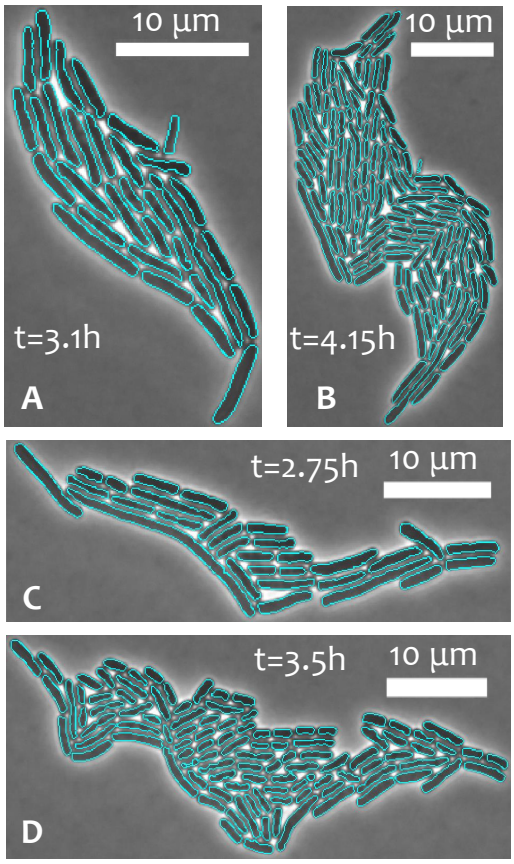

FIG. S6. **Quantifying cell aspect ratio.** The comparison of AR at early and late time points in a growing colony of Strain-1, shown in **(A)** and **(B)** respectively, for 30°C. Corresponding observation for Strain-2 is given in Panels **(C)** and **(D)**. One time point is selected that is much before the MTMT event (younger generation) while the other selected time point is just before MTMT occurrence. We segmented the cells and estimated the mean AR at the two time points for each strains. For Strain-1, panels A and B has mean AR of 4.24 and 3.67. For Strain-2, panels C and D have mean AR of 4.18 and 2.92. Thus, the AR decreases as one approaches MTMT. In relation to the accompanying topological defects (Figure **??**), Strain-1 with mean AR ~ 5.26 has $6 < N_d < 8$ defects, while Strain-2 with mean $AR \sim 4.1$ shows $8 < N_d < 11$ defects.

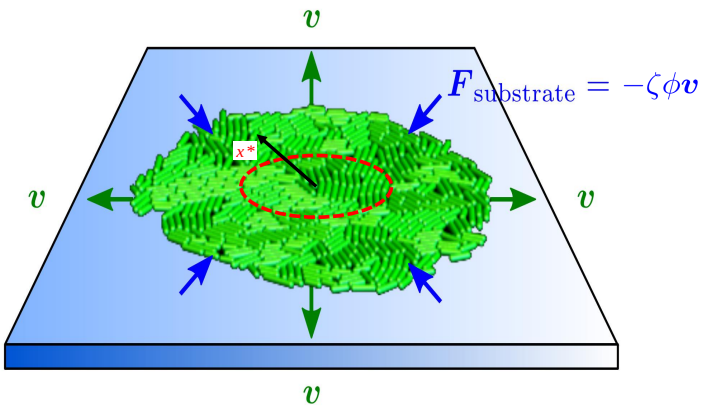

FIG. S7. **P-zone and force balance in an expanding bacterial colony.** Schematic representation of the expanding colony underlying our continuum model. The colony grows isotropically under the active forces originating from cell division. Its expansion, however, is hindered by the drag force $\boldsymbol{F}_{\text{substrate}} = -\zeta\phi\boldsymbol{v}$, with ζ a constant, ϕ the cell packing fraction and $\boldsymbol{v}$ the local velocity, resulting from the cell-substrate interactions. As a consequence of this obstruction, the cell density around the colony center increase with time, eventually exceeding the critical pressure $P_c = f_c/A_{\text{cap}}$ with f_c given in Eq. **??**. This gives rise to an increasingly large region, named P-zone in Ref. [3], where a cell division will immediately lead to the MTMT event. For PDF of the extrusion cites ($|x^*|$) as a function of the distance from the colony centre, please see Ref. [3].

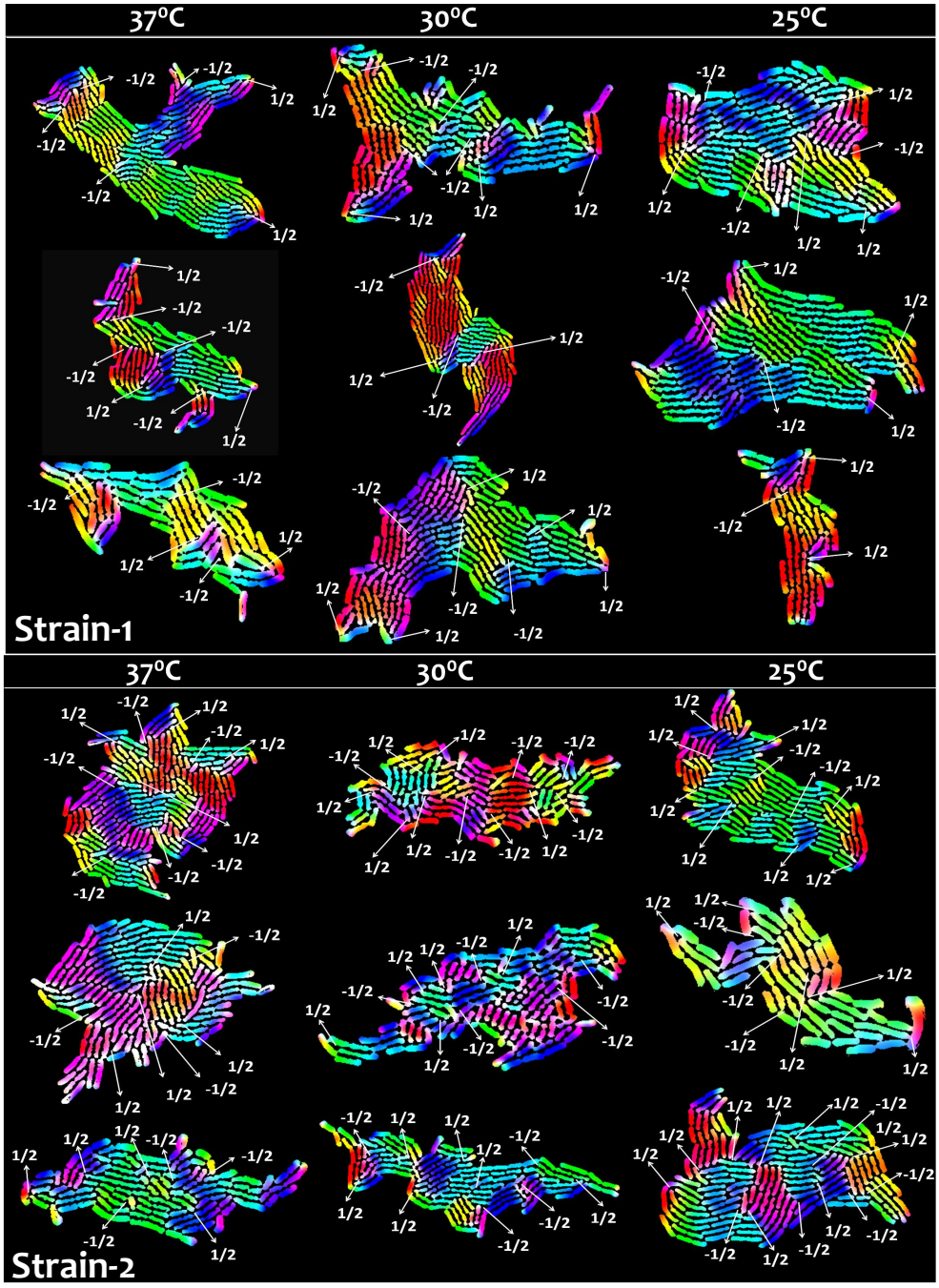

FIG. S8. **Extracting topological defects at the MTMT event.** The montage of the defects at MTMT in each of the strains for each replicates and temperature. The details of the image and orientational analysis is described in Section **??**. At MTMT, the number of topological defects and it's density (normalized by the colony area) in a given species remain nearly same across all temperatures considered here. However, the rate of production of defects from $t = 0$ and $t = t_c$ increase with the growth temperature (i.e., activity). It is worth noting here that the temperature-dependent rates of colony and cell length expansions at MTMT trigger differences in the domain formation pattern, and consequently, of the ensuing topological defect number and their locations. The results show that at t_c the number of defects remains same across all temperatures. However, since $t_c \sim T^{-1}$, the time-averaged rate of defect formation at the onset of MTMT goes up with the T. Microdomain formation and evolution of defects closely mediate the onset of the MTMT event.

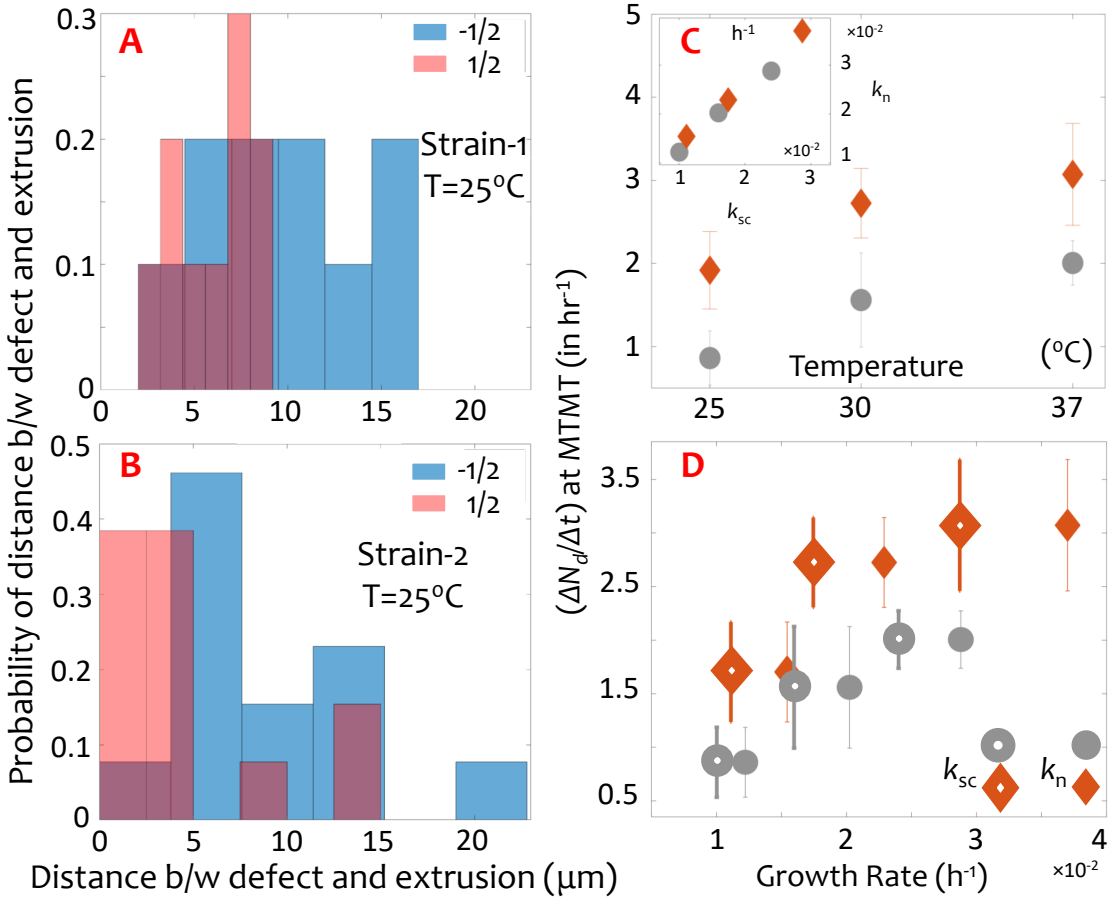

FIG. S9. **Distance between topological defects and the site of the 2D to 3D extrusion event.** The probability of the occurrence of an extrusion event around a topological defect is plotted for 25°C of **(A)** Strain-1 and **(B)** Strain-2 over the separation between the extrusion site and neighbouring topological defects (both + and − defects are considered). We observe that the probability of occurrence of an extrusion event around a $+1/2$ defect is higher relative to a $-1/2$ defect. The nature and presence of topological defects reveals an underlying spatial correlation between the defect and extrusion sites (will be discussed elsewhere). Similar observation have been reported previously for other forms of active confluent systems [23–26]. Inset **(C)**: The cell elongation rate (log(2)/(doubling time)) varies linearly with the population growth rate (see Supplementary Figure S3). The average rate of defect production between $t = 0$ and $t = t_c$ increases monotonically with the **(C)** growth temperature and **(D)** growth rate.

[1] Campos, M. *et al.* A constant size extension drives bacterial cell size homeostasis. *Cell* **159**, 1433–1446 (2014).

[2] Amir, A. Cell size regulation in bacteria. *Physical Review Letters* **112**, 208102 (2014).

[3] You, Z., Pearce, D. J. G., Sengupta, A. & Giomi, L. Mono- to multilayer transition in growing bacterial colonies. *Physical Review Letters* **123**, 178001 (2019).

[4] Ottino-Loffler, B., Scott, J. G. & Strogatz, S. H. Evolutionary dynamics of incubation periods. *eLife* **6**, e30212 (2017).

[5] Hosoda, K., Matsuura, T., Suzuki, H. & Yomo, T. Origin of lognormal-like distributions with a common width in a growth and division process. *Physical Review E* **83**, 031118 (2011).

[6] Wallden, M., Fange, D., Lundius, E. G., Özden Baltekin & Elf, J. The synchronization of replication and division cycles in individual e. coli cells. *Cell* **166**, 729–739 (2016).

[7] Hashimoto, M. *et al.* Noise-driven growth rate gain in clonal cellular populations. *Proceedings of the National Academy of Sciences* **113**, 3251–3256 (2016).

[8] Ackermann, M. A functional perspective on phenotypic heterogeneity in microorganisms. *Nature Reviews Microbiology* **13**, 497–508 (2015).

[9] Levchenko, A. & Nemenman, I. Cellular noise and information transmission. *Current Opinion in Biotechnology* **28**, 156–164 (2014).

[10] Wada, T., Hironaka, K. & Kuroda, S. Cell-to-cell variability serves as information not noise. *Current Opinion in Systems Biology* **27**, 100339 (2021).

[11] Sharma, D., Misba, L. & Khan, A. U. Antibiotics versus biofilm: an emerging battleground in microbial communities. *Antimicrobial Resistance & Infection Control* **8**,

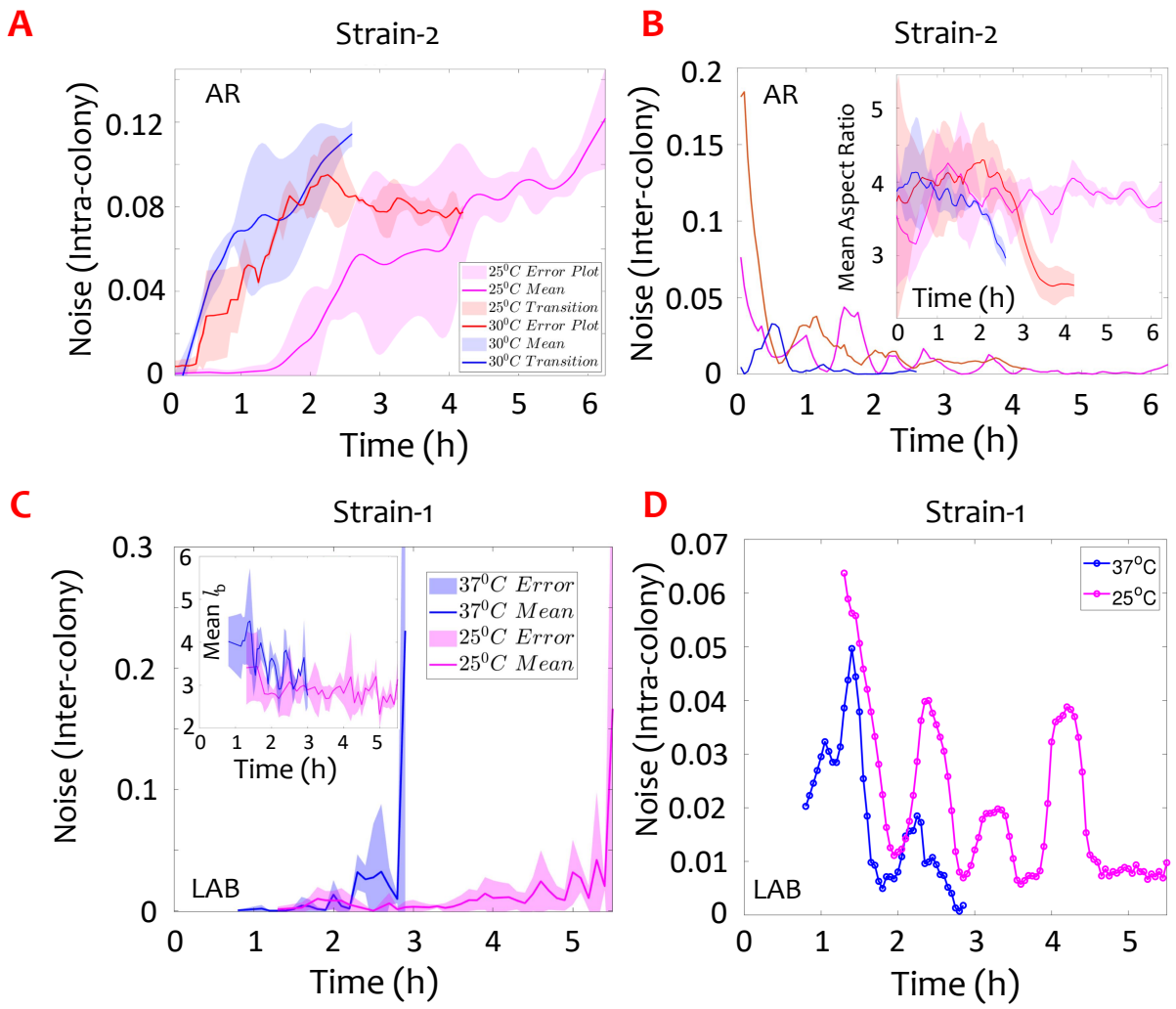

FIG. S10. **Temporal variation of** AR **and length-at-birth (ℓ_b) noise at individual and colony scales. (A)** Temporal variation of cell-cell AR noise within Strain-2 colonies. Shaded region presents error about the mean AR in the colony. **(B)** Temporal variation of AR inter-colony noise for Strain-2 for different temperatures, computed from the variance across three biological replicates. Inset: The temporal variation of the mean and error of the AR across colonies. **(C)** Temporal variation of cell-cell LAB (ℓ_b) noise within Strain-1 colonies (Strain-2 shows similar variation, not shown for the sake of brevity) for 25°C and 37°C. Inset: The temporal variation of the mean and error of ℓ_b across the colonies. **(D)** Temporal variation of AR inter-colony noise for Strain-2 for 25°C and 37°C, computed from the variance across three biological replicates.

1–10 (2019).

[12] Palková, Z. & Forstová, J. Yeast colonies synchronise their growth and development. *Journal of cell science* **113**, 1923–1928 (2000).

[13] Shrivastava, A. *et al.* Cargo transport shapes the spatial organization of a microbial community. *PNAS* **115**, 8633–8638 (2018).

[14] Chen, T. *et al.* Self-organization of tissue growth by interfacial mechanical interactions in multilayered systems. *Advanced Science* 2104301 (2021).

[15] Heisenberg, C.-P. & Bellaïche, Y. Forces in tissue morphogenesis and patterning. *Cell* **153**, 948–962 (2013).

[16] Finkelshtein, A., Roth, D., Jacob, E. B. & Ingham, C. J. Bacterial swarms recruit cargo bacteria to pave the way in toxic environments. *mBio* e00074–15 (2015).

[17] Muok, A. R., & Briegel, A. Intermicrobial hitchhiking: How nonmotile microbes leverage communal motility. *Trends in Microbiology* **29**, 542–550 (2021).

[18] Shklarsh, A. *et al.* Collective navigation ofcargo-carrying swarms. *Interface Focus* **2**, 786–798 (2012).

[19] Dogra, N., Izadi, H. & Vanderlick, T. K. Micro-motors: A motile bacteria based system for liposome cargo transport. *Scientific Reports* **6**, 29369 (2016).

[20] Tran, F. & Boedicker, J. Q. Genetic cargo and bacterial species set the rate of vesicle-mediated horizontal gene transfer. *Scientific reports* **7**, 1–10 (2017).

[21] Yu, Z. *et al.* Hitchhiking behavior in bacteriophages facilitates phage infection and enhances carrier bacteria col-

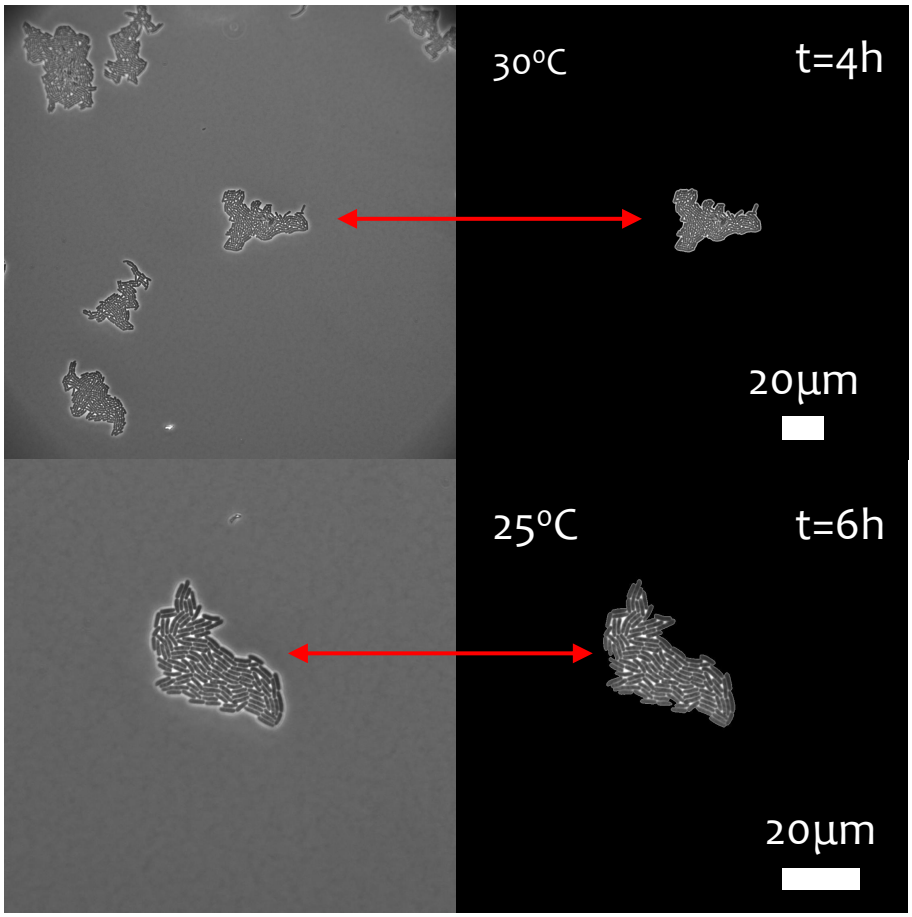

FIG. S11. **Single colony extraction for PIV analysis.** A pre-processing is performed prior to the PIV analysis. The two important aims of the analysis are to segment out the background in order to remove any undesired background effects (for instance, particulates), and to detect a single colony to study its growth. Variations in brightness levels can incorporate unwanted noise in the PIV results, thereby rendering the prediction in the local hydrodynamic and transport activity erroneous. In order to reduce errors, single colonies were cropped and analyzed (simultaneous multi colony analysis was not aimed at in the present study). For the purpose of colony extraction, a threshold is applied and area of different labels are extracted from their region properties. Connected area at a particular selected location where a particular point is encompassed (a point chosen on a first cell) is labelled out. This is done across all time steps to extract the bacterial colony. Hereon, the PIV technique is applied on the evolving bacterial colony. The results obtained from PIV pre-processing analysis is given in Supplementary section D (**Movie S1** B, E and H for 37°C, 30°C and 25°C, respectively.). Post-PIV one obtains a field of flow quantities like velocity, vorticity, strain rate which are computed to an accuracy equal to the floating point accuracy of the system. Since such small differences are indistinguishable in experiments, we set a minimum detection threshold of 10^{-5}rad-s^{-1} for the vorticity, that emerges from scaling arguments. Since the characteristic speed of the colony growth falls in the order of 10^{-9}m-s^{-1}, and the relevant length scale is in the order of 1 μm, a vorticity scale of 10^{-3}rad-s^{-1} is arrived at. Conservatively, we set our threshold two orders lower to track physically distinguishable vortices. With this consideration, we extract the number of unique vortices (all vortices of the same value when the above vorticity cut-off is applied) from the PIV results and plot it against time.

onization. *Environ. Sci. Technol.* **55**, 2462–2472 (2016).
[22] Hiratsuka, Y., Miyata, M., Tada, T. & Uyeda, T. Q. P. A microrotary motor powered by bacteria. *PNAS* **103**, 13618–13623 (2006).
[23] Saw, T. B. *et al.* Topological defects in epithelia govern cell death and extrusion. *Nature* **544**, 212–216 (2017).
[24] Grobas, I., Polin, M. & Asally, M. Swarming bacteria undergo localized dynamic phase transition to form stress-induced biofilms. *eLife* **10**, 1325–1334 (2021).
[25] Turiv, T. *et al.* Topology control of human fibroblast cells monolayer by liquid crystal elastomer. *Science Advances* **6** (2020).
[26] Guillamat, P., Blanch-Mercader, C., Kruse, K. & Roux, A. Integer topological defects organize stresses driving tissue morphogenesis. *bioRxiv* (2020).

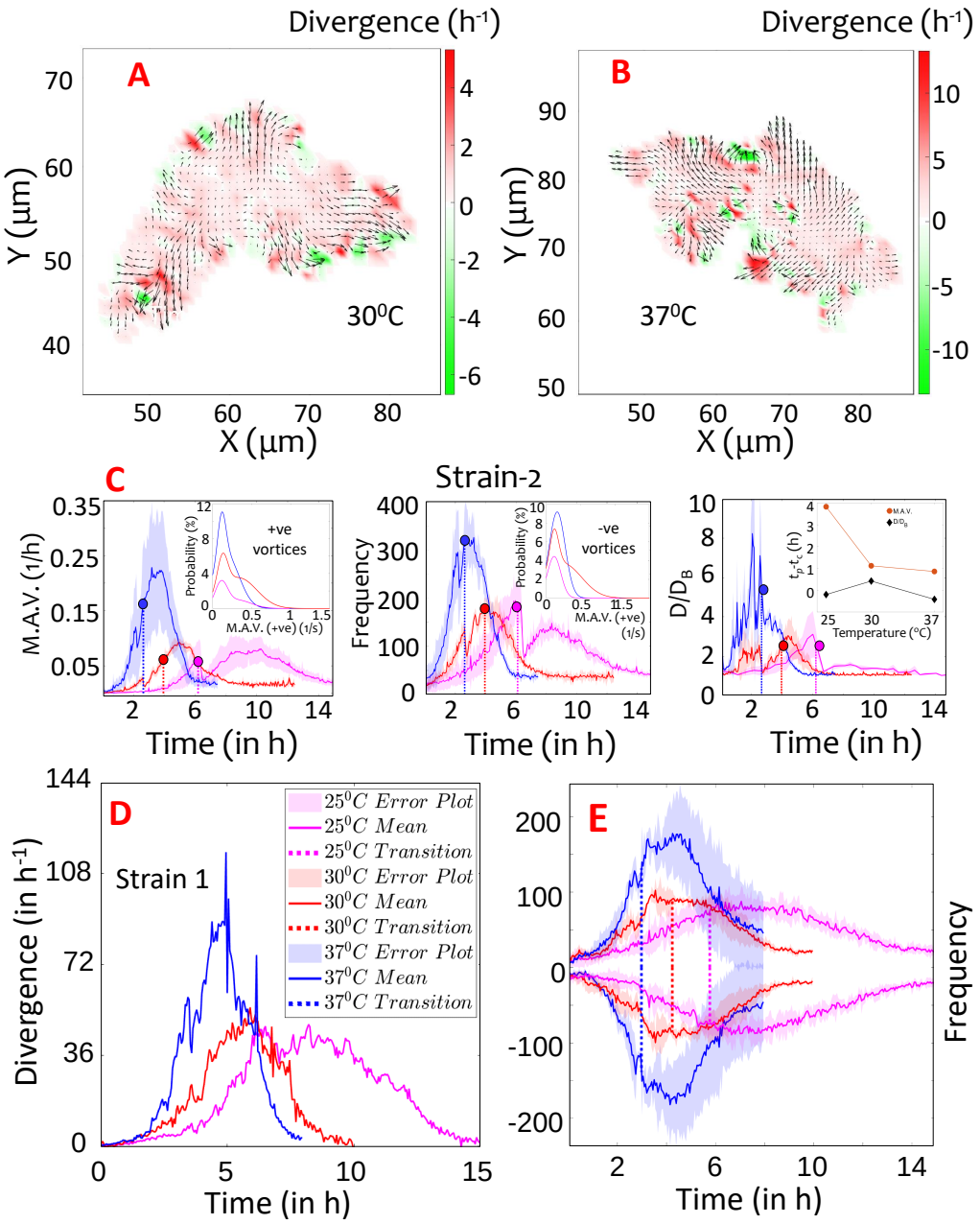

FIG. S12. **Divergence and vortex distribution at MTMT. (A)** and **(B)** The divergence field distribution at 30°C and 37°C, respectively. The divergence strength, as depicted in the colormap, shows strong correlation with the culture temperature. Higher temperature results in a stronger colony and cell growth (Fig S1) and therefore stronger divergence. The colony specification are corresponding to Fig 3A of the main draft. All dimensions are in microns. **(C)** Mean absolute vorticity (first column), the number of unique vortices (second column) and the effective diffusion ratio (third column) for Strain-2. The insets in panel **(C)** depicts the phase-plot of positive and negative vortex distribution for Strain-2. **(D)** The mean divergence of a colony is always greater than 0, a signature of an expanding colony. Furthermore, the strength of the divergence decreases with decrease in temperature. Thus quantitatively, the colony activity as a whole regulates the hydrodynamics, both of which can be regulated by the temperature. The trend is same for both the strains across all temperatures, so only a single data is depicted in the figure. **(E)** Distribution of frequency of positive (anticlockwise) and negative (clockwise) vortices as function of colony age. The figure depicts that the distribution of such vortices are nearly equal across the colony age. This figure is the break-up of Figure **??** presenting the frequency of vortices which gives the total count including both positive and negative vortices. Unique vortices show the perturbations within the system by enumerating the amount of microscale vortices that form due to the colony growth. The results are consistent with the mean absolute vorticity, however, the predictive capability of colony transition seems more accurate with unique vortices representation and remains consistent across strains and temperature of the colony growth. The peak of each of the plots lie close to the transition time (dashed line) of the corresponding colour. Supplementary section D **Movie S1** C, F and I show the time evolution of velocity magnitudes for 37°C, 30°C and 25°C.

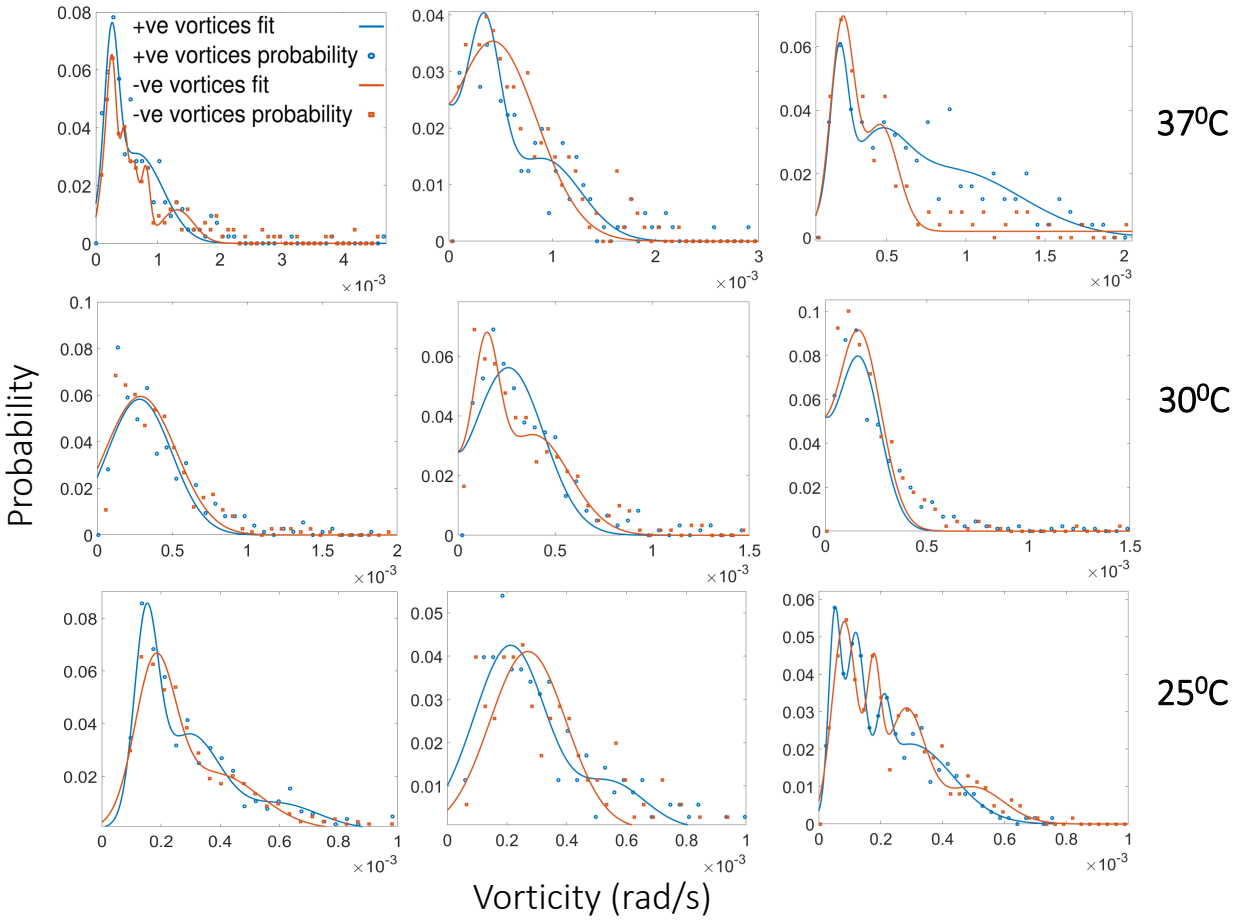

FIG. S13. **Log-normal distribution of vortices in a colony at MTMT.** Distribution of phase plots of vorticity strength probability distribution for Strain-1 for each temperature and experimental replicate just before MTMT. A general observation of log-normal distribution of vortex strength is noted. Alongside, the log-normal distributions of the cell aspect ratio (Figure **??**), the distribution of the vortex strengths allow us to connect the topology in structure and active hydrodynamics, thereby revealing a global time-synchrony of the topological features at time of MTMT. Albeit locally, the cell aspect ratio and vortex strength may remain uncorrelated, our results elucidate links between the topological structure of the active nematic phase and the geometry of the emergent flow fields. An expanding confluent bacterial colony thus represents a dynamical multifield topological system where the individual and colony geometry, and the active hydrodynamic flows–both in the colony and its micro-environment–remain temporally and spatially correlated due to the underlying topological attributes of this dynamical system.

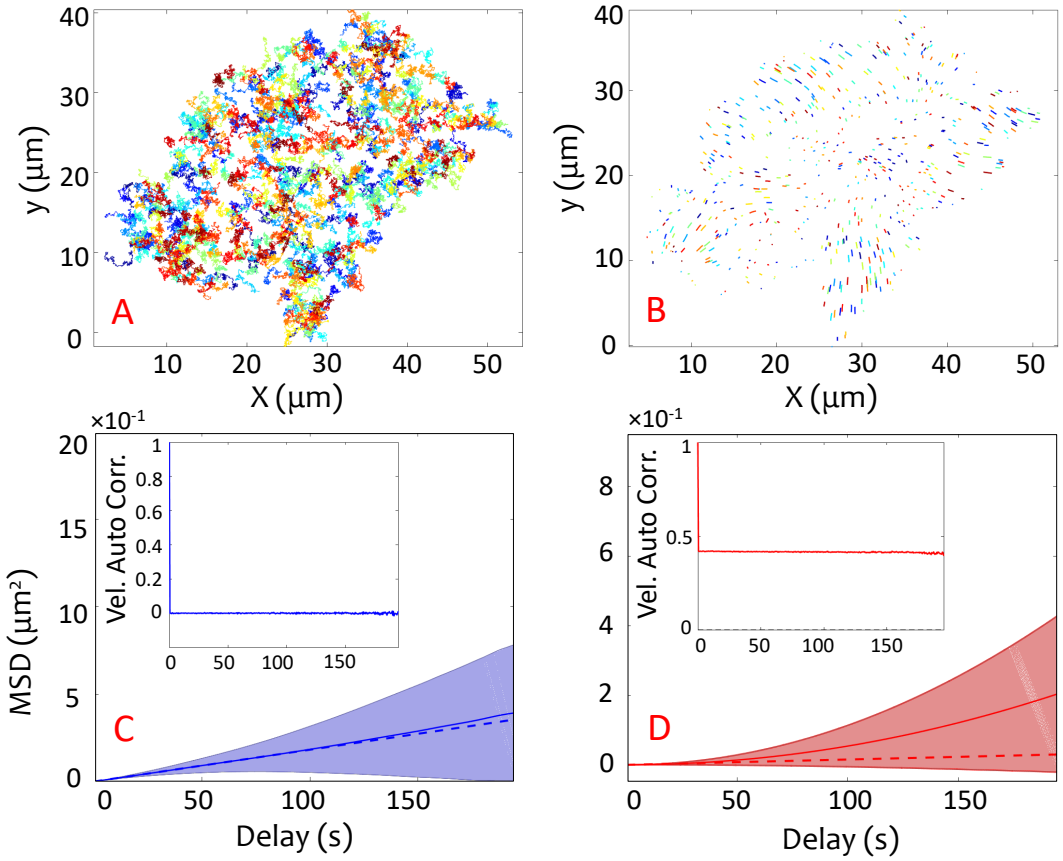

FIG. S14. **Simulated tracks of passive particles from the experimental PIV data.** **(A)** and **(B)** The particle tracks due to colony expansion corresponding to Figure (C) and (D), left and right column respectively. The MSD is derived from these tracks. Panel A shows that the tracks are random which is a signature of strong Brownian motion. Since this corresponds to lower viscosity and particle radius, the Brownian forces are dominant while the fluid momentum transfer from colony motion to the suspended passive particles is suppressed. **(C)** and **(D)** The result of two corresponding MSD analysis and the corresponding velocity correlation of the above trajectories at two different combination of radius-viscosity situation are provided. For larger particles and higher viscosity, the Brownian motion is outweighed by the momentum generated by the colony expansion. As shown earlier, enhancement of the active transport ($(D/D_B)_{z=z_1}$) depends on temperature-mediate activity, physical dimension of transported entity and the local viscosity. With a drop in activity, colony hydrodynamics–and consequently the local transport in the vicinity–reduces, thus limiting a population's ability to take up, for instance, nutrients (to grow optimally), and thus forming an active feedback loop.

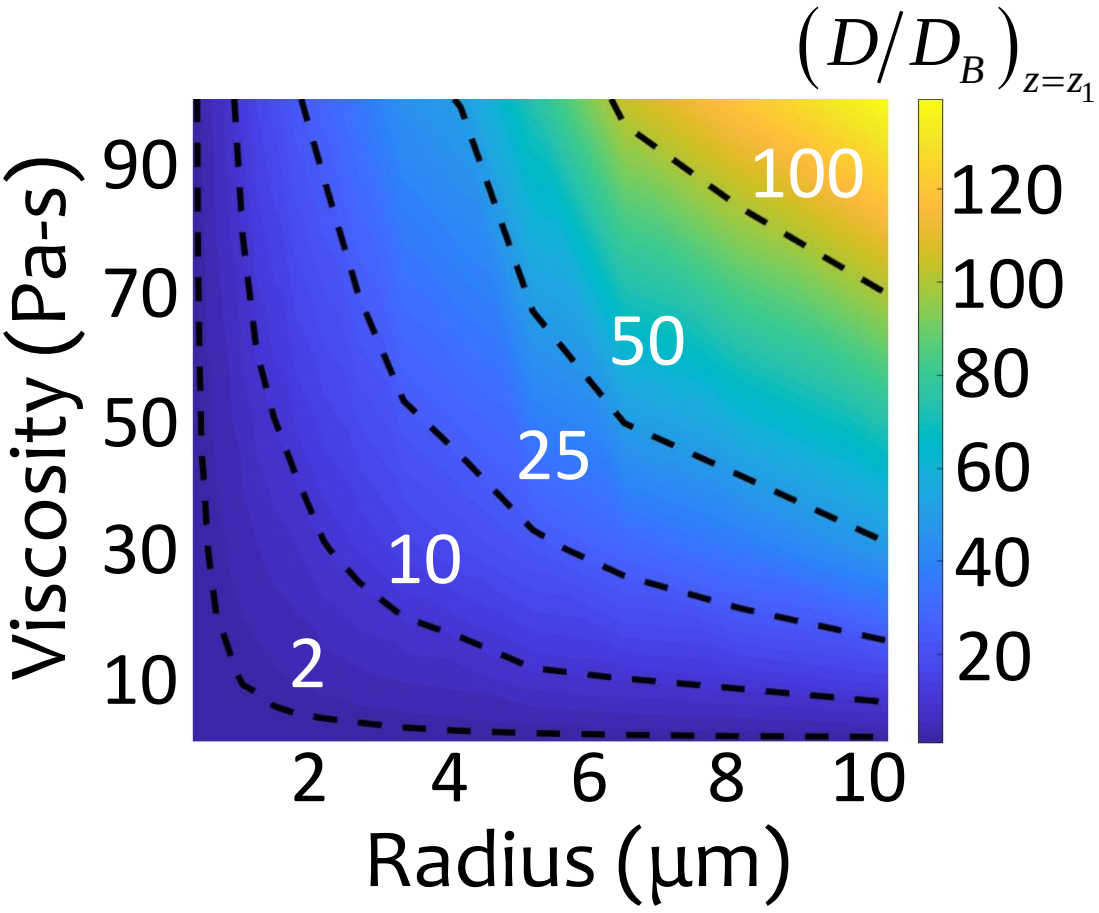

FIG. S15. **Phase-plot of first layer relative diffusion strength from data-driven simulations.** Experimental data-driven simulated transport of passive micro-cargo by expanding confluent colonies shown as a phase-plot of $(D/D_B)_{z=z_1}$ using the mean squared displacement analysis. The gain in the diffusive transport, for a given bacterial activity, is computed by varying the passive particle dimensions and local viscosity. The contour of the gain ratio is delineated using the dotted-black lines with corresponding values in white. High viscosity and particle dimension renders active transport more effective than the Brownian diffusion.

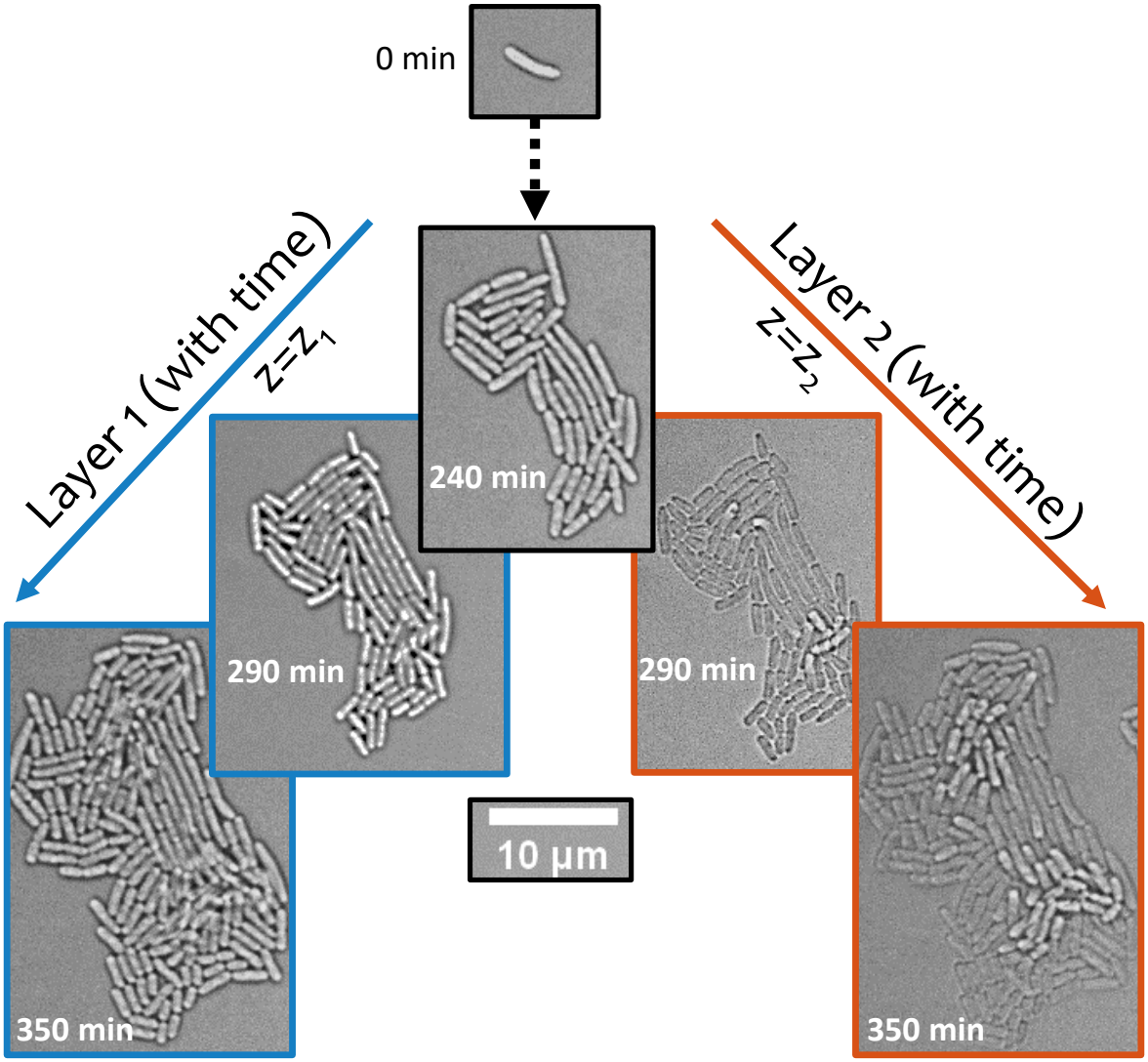

FIG. S16. **Diffusion as projected in the third dimension with MTMT.** Timeline of colony growth in the first and second layer. The layers are captured by focusing on each bacterial plane. The individual layers are extracted and analysed using PIV (Methods). The results from PIV provided us with the U, V-velocity field for each plane. Applying a no-slip boundary condition and continuity equation $\nabla \cdot \boldsymbol{v}$, we obtain the W-component of the velocity field for the first layer. Knowing the velocity of the first layer and using the above constraints, the velocity of the second layer, after MTMT, is approximated Figure **??**B. The U, V-velocity field is also used to compute the local diffusion coefficient for each layer Figure **??**B.

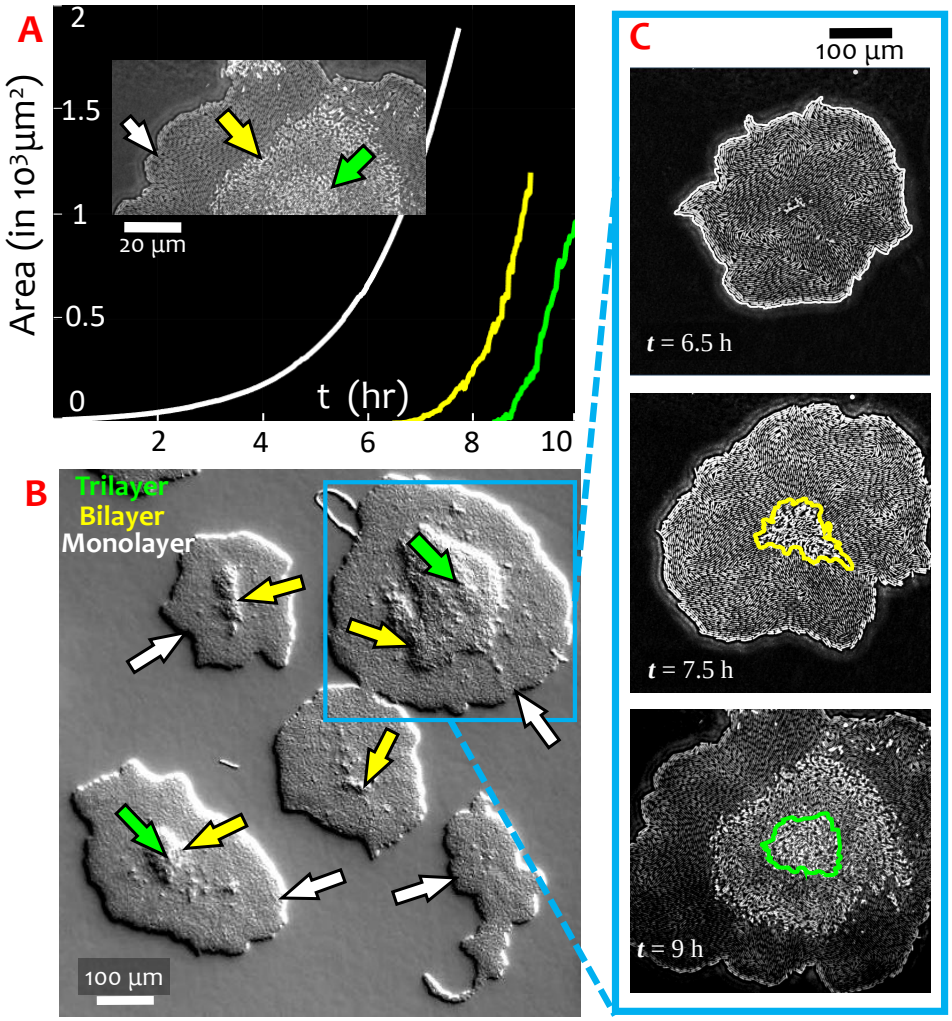

FIG. S17. **Extrusion of monolayer to multiple layers. (A)** The growth of the mono- (white), bi- (yellow) and tri- (green) layers show different expansion rates, captured in a $A(t)$ plot, following the colour scheme in panel **(B)**. The inset in **(A)** shows the zoomed-in micrograph of all three layers, the entire colony and expanding layers are shown in panel **(C)**. Once the colony transitions to the second layer, both the first and second layers continue expanding, however with different areal speeds. The second layer expands faster than the first layer; and upon extrusion of the third layer, the third layer expands faster relative to each of the first and second layers. As more layers continue adding up, the areal speed diminishes progressively, while the colony expansion continues in the vertical plane. Ultimately, the net horizontal expansion is arrested, and the bacterial colony develops primarily in the vertical plane.

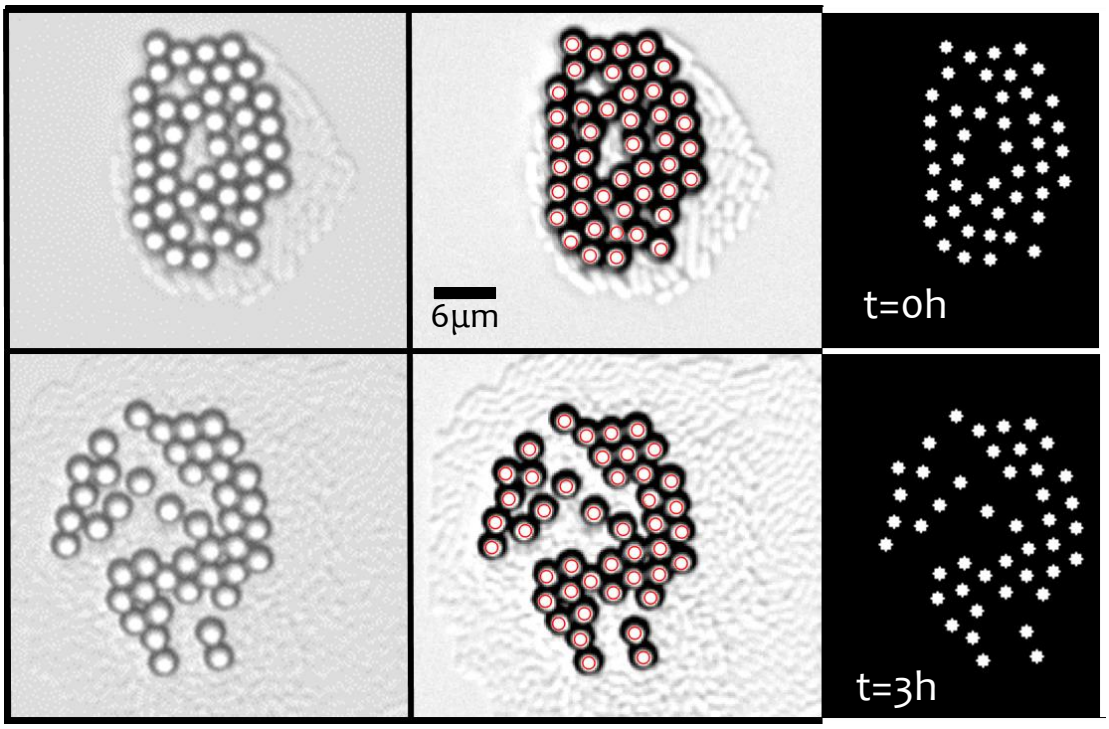

FIG. S18. **Identification and trajectory analysis of passive micro-cargo advected by a growing colony.** Experimental visualization of microscale transport induced by a growing bacterial colony at 30°C. The upper row delineates the initial position of the beads and their corresponding identification and segmentation. The beads are identified and extracted using a combination of MATLAB and Ilastik packages. The second panel shows the final position of the beads after 3 hours from the point of initial visualization. The trajectories we analyzed to obtain the effective diffusion coefficient employing the mean squared displacement method. One practical observation that attracted our attention is the ability of the apparently weak bacterial motion to de-cluster passive 2 μm particles, which otherwise remain strongly aggregated if only Brownian motion persists (control case, without bacterial colonies). A video on the evolution of the bead position for a particular colony (for 37°C and 25°C) is provided in the Supplementary section D (**Movie S2**).

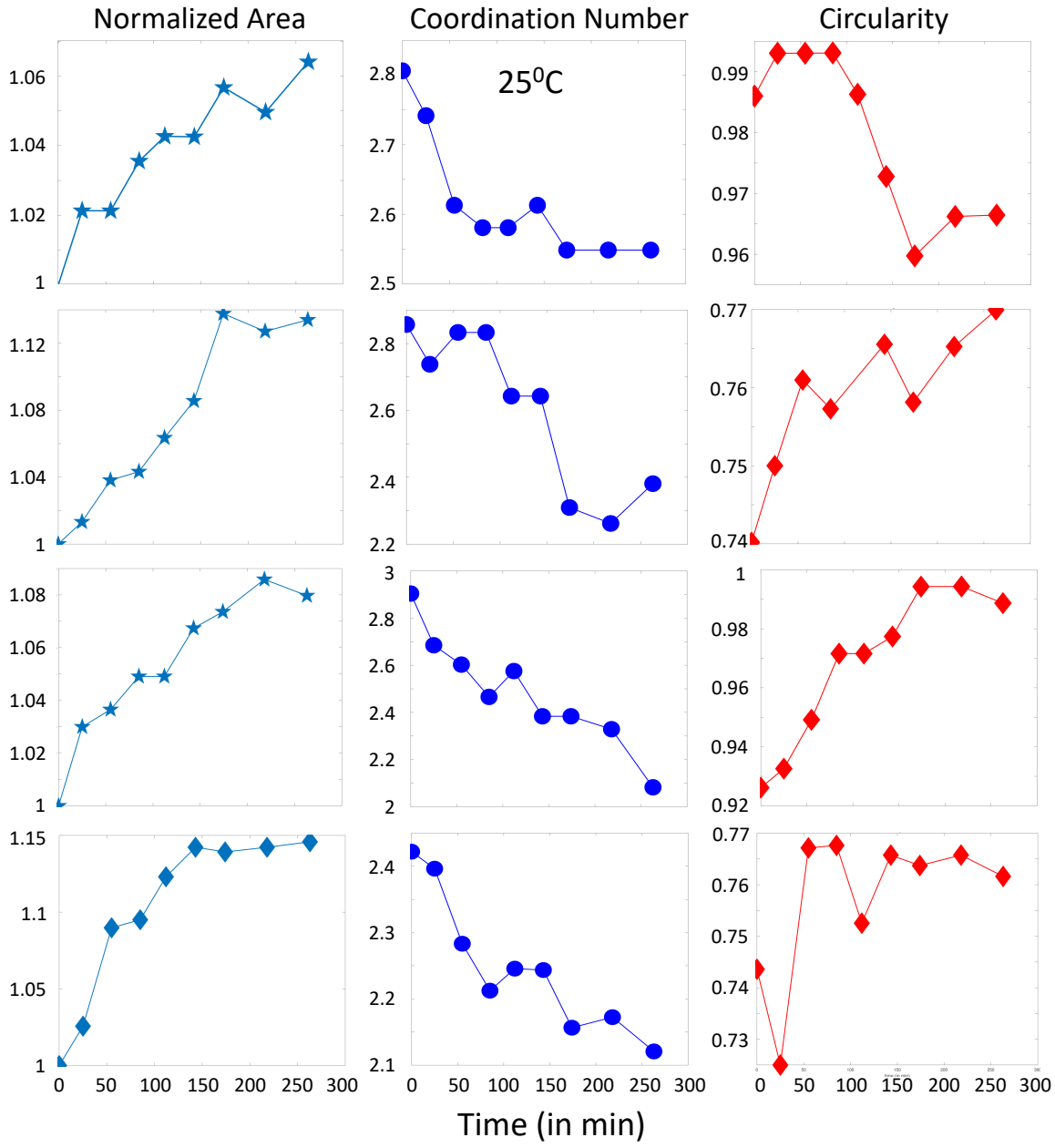

FIG. S19. **Quantifying de-clustering of tracer particles over time.** Time evolution of normalized area (A_p), coordination number (CN), and circularity (ratio of short and long axis of enveloping ellipse, b/a) of a de-clustering event of aggregated particles at 25°C. The normalized area is computed as a ratio of area of the ellipse bounding the tracer cluster at a given time, over the bounding area when the measurement started. The circularity at a given time point is computed by taking the ratio of the lengths of the minor and major axes of the bounding ellipse (b/a). Each row indicates one biological replicate. By plotting the circularity of the tracer constellation over time, we obtain a qualitative measure of the momentum transferred from the confluent colonies to the suspended particles. The circularity increases initially, however plateaus below 1 (Figure S21). A final value ∼1 would suggest that the momentum gets isotropically transferred to the passive micro-cargo.

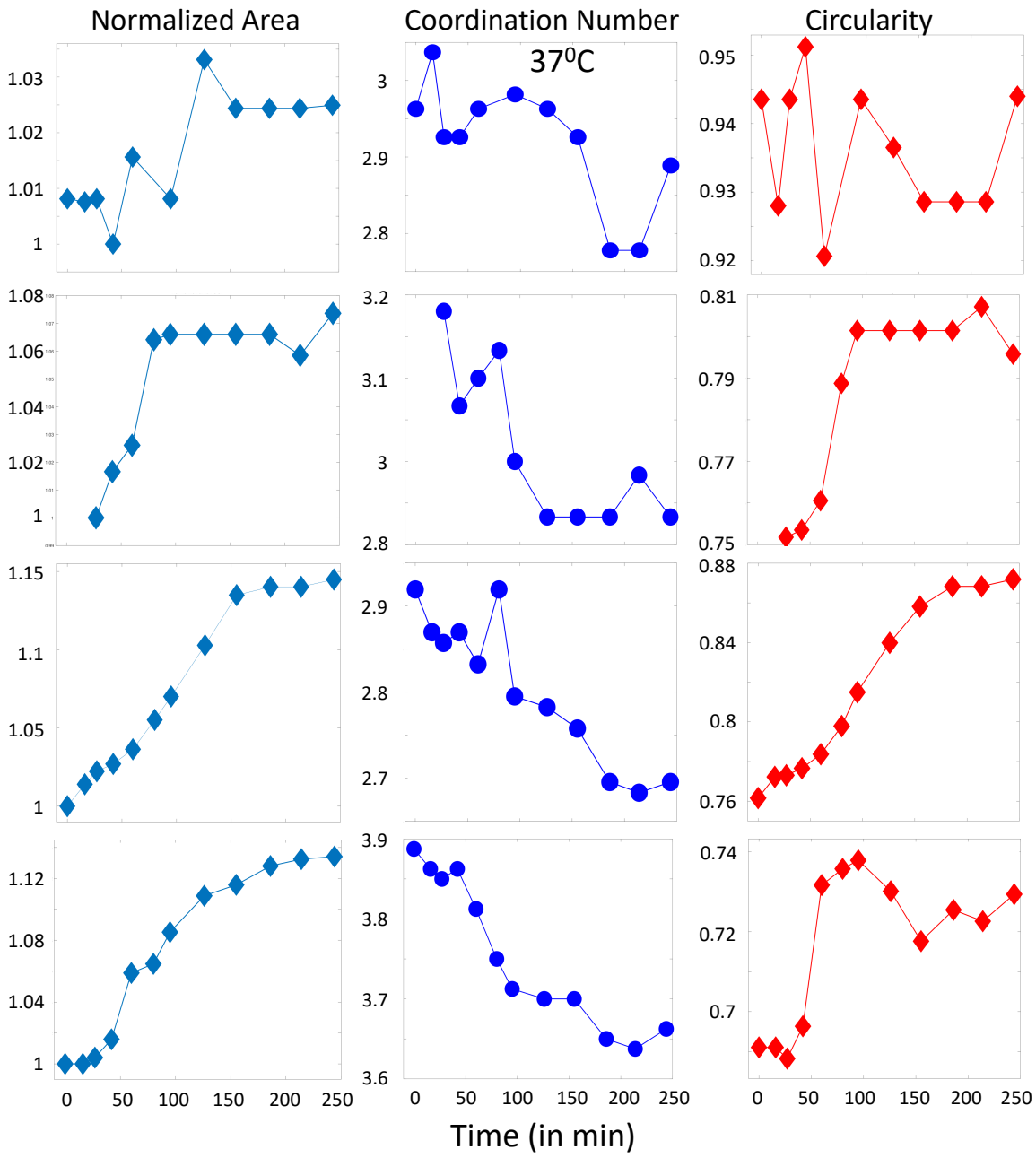

FIG. S20. **De-clustering of tracer particles over time at 37°C.** Following up from the Figure S19, here we show the time evolution of the normalized area, coordination number and circularity passive micro-cargo cluster at 37°C. Each row indicates one biological replicate. Higher activity at 37°C induces stronger micro-environmental transport. The circularity is defined as the ratio between the lengths of the minor and major axes of the bounding ellipse (see Figure S21).

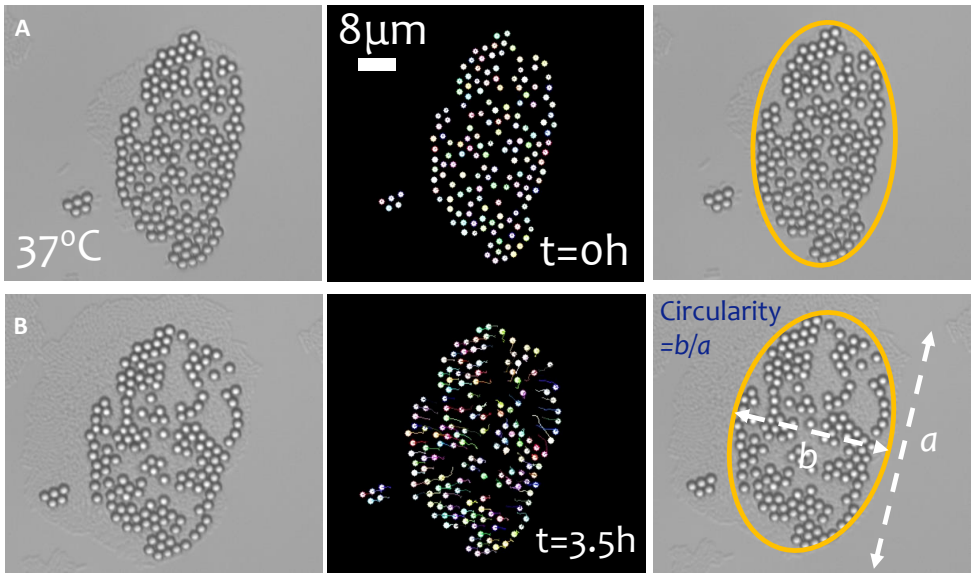

FIG. S21. **Transport-driven geometrical evolution of tracer clusters.** **(A)** Initial cluster of tracer particles in the vicinity of bacterial colony, shown as phase contrast (left panel) and binarized (middle panel) images. The right panel presents the bounding ellipse using which the geomteric circularity is computed. The circularity is defined as the ratio between the lengths of the minor and major axes of the bounding ellipse (b/a). **(B)** Geometry of de-clustered tracer particles after 3.5 h, captures the change in the circularity, along with the transport-driven divergence of the de-clustered particles.